Supporting Information

Bond Modulation of $MoSe_{2+x}$ Driving Combined Intercalation and Conversion Reactions for High-Performance K Cathode

Ting Lei,‡ Mingyuan Gu,‡ Hongwei Fu, Jue Wang, Longlu Wang, Jiang Zhou, Huan Liu, and Bingan Lu*

CONTENTS

Section 1. Experimental Procedures

Synthesis of pure $MoSe_{2+x}$, $MoSe_{2+x}$-rGO and $MoSe_2$-rGO. $MoSe_{2+x}$-rGO was prepared using a one-step hydrothermal method. Sodium molybdate was used as the Mo source and selenium powder was used as the Se source. Hydrazine hydrate played an important role in the formation of hydrazine-Se and the efficient reduction reaction of Se and MoO_4^{2-}. In a typical procedure, 2 mmol of sodium molybdate (Na_2MoO_4, GHTECH) was dissolved in 20 mL of deionized water. In a separate beaker, 6 mmol of selenium powder (Se, Aladdin) was added to a mixture of 15 mL of a hydrazine hydrate solution ($N_2H_4 \cdot H_2O$, 80%, Sinopharm) and 20 mL of 5 mol mL^{-1} graphene oxide aqueous solution (GO, Tanfeng Tech), and stirred for at least one day. Then, the Na_2MoO_4 solution was poured into the mixture, which was transferred into a Teflon-lined autoclave and heated in an oven at 180 °C for 12 h. The as-obtained black solid was separated by filtration, washed with deionized water and ethanol several times, and dried at 60 °C under vacuum for one night to produce $MoSe_{2+x}$-rGO. The $MoSe_{2+x}$ was prepared in the same way without the addition of GO. For comparison, well-crystallized $MoSe_2$-rGO was synthesized by annealing $MoSe_{2+x}$-rGO at 450 °C under pure argon (Ar) for 10 h.

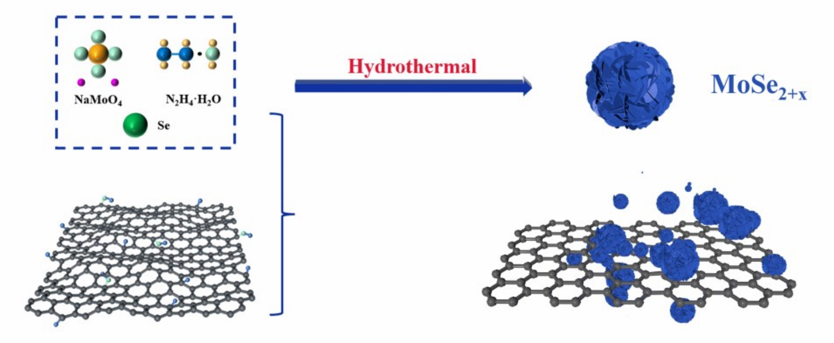

Figure S1. Schematic illustration of the synthesis of $MoSe_{2+x}$-rGO.

Section 2. Characterization Methods

Pure $MoSe_{2+x}$, $MoSe_{2+x}$-rGO and $MoSe_2$-rGO structures were characterized by an X-ray diffractometer (Bruker D8 ADVANCE with Cu Kα irradiation (λ = 1.5406 Å), and the Raman spectra were taken by Renishaw's inVia Raman (488 nm). The morphology and components of $MoSe_{2+x}$-rGO and $MoSe_2$-rGO were characterized via FESEM (Hitachi S-4800) and AC-TEM (Titan G2 60-300) with EDS and element distribution analysis. The chemical states of $MoSe_{2+x}$-rGO and $MoSe_2$-rGO samples were analyzed by XPS (Thermo Fisher Scientific ESCALAB 250Xi). Thermogravimetric analysis was carried out using a Thermo-Gravimetric Analyzer (TGA, PerkinElmer, Diamond TG/DTA) in air from room temperature to 800 °C. Brunauer–Emmett–Teller (BET) analysis of the surface area and pore size distribution of $MoSe_{2+x}$-rGO and $MoSe_2$-rGO were obtained using Quabrasorb SI-3MP.

Section 3. Assembling and Testing Methods

Electrochemical properties were evaluated by assembling 2032 coin-type cells in a highly pure argon-filled glove box (O_2 and H_2O levels below 0.01 ppm). The half cell was assembled with K/Li metal as the counter electrode and a fiberglass paper as the separator. The working electrode consisted of 80 wt% as-synthesized sample ($MoSe_{2+x}$-rGO, $MoSe_2$-rGO and pure $MoSe_{2+x}$), 10 wt% Super P and 10 wt% poly (vinylidene fluoride) (PVDF) binder with carbon coated aluminum foil as the current collector. The average mass loading of the electrodes is around 1 mg cm^{-2}. The electrolyte for PIBs consisted of 3.0 M potassium bis(fluorosulfonyl)imide (KFSI) salt in dimethoxyethane (DME) solvent for room temperature tests, and 1,1,2,2-tetrafluoroethyl-2,2,3,3-tetrafluoropropylether (TTE) with the volume ratio of 1% in 0.5 M potassium hexafluorophosphate (KPF_6) salt in DME solvent for low temperature tests (-20 °C). The electrolyte for LIBs consisted of 4.0 M lithium bis(fluorosulfonyl)imide (LiFSI) salt in DME solvent. For full cell, the cathode was as same as the working electrode above, the anode was the nano graphite. The anode was first assembled into a half cell for pre-cycling to eliminate its irreversible capacity loss before matching the full cell. The electrolyte of full cell is the same as that of half-cell. The ratio of capacity per unit area for the anode and the cathode was around at 1.12. The mass loading of anode and cathode was 1.03 and 1.68 mg, respectively. The capacity of full cell was calculated on the mass of cathode. The CV curves and the nyquist plots were recorded using a CHI660e electrochemical work station at the scan rate from 0.1 to 1.5 mV s^{-1} and the frequencies ranging from 10^{-2} to 10^5 Hz, respectively. The cycle, rate and GITT tests were performed using the Neware BTS-53 system and Land-CT2001A in the voltage range of 0.5 to 3.0 V (vs. K/K^+).

Section 4. Computational Methods

Density functional theory (DFT) calculations were performed with the Vienna Ab-initio Simulation Package (VASP) code.[1, 2] The generalized gradient approximation (GGA) in the form of the Perdew-Burke-Ernzerhof (PBE) functional with a cut-off energy of 500 eV were selected to describe the exchange-correlation term.[3, 4] For structural optimization, the Gamma-Centered k-points was set as 3 × 3 × 2 for $MoSe_{2+x}$ and 3 × 3 × 2 for $MoSe_2$, respectively. The convergence criterion for the energy and maximum force for the optimization were set 10^{-5} eV and 0.02 eV $Å^{-1}$, respectively. To incorporate the long-range van der Waals interactions, a dispersion correction of the total energy (DFT-D4 method) was adopted.[5]

Section 5. Characterizations of $MoSe_{2+x}$-rGO, pure $MoSe_{2+x}$ and $MoSe_2$-rGO

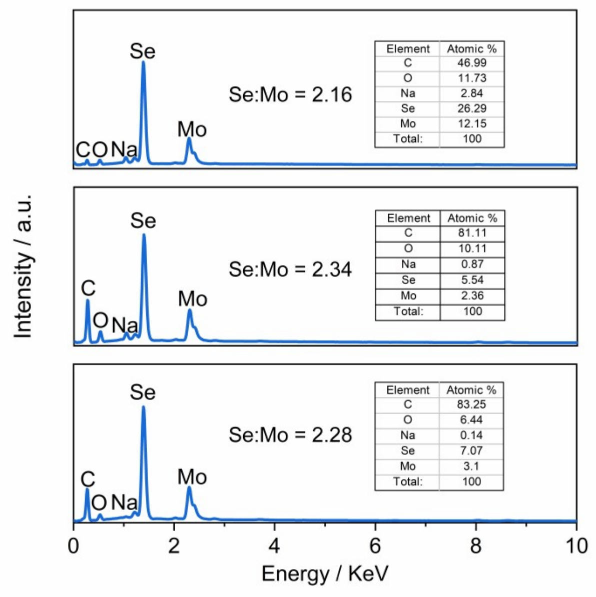

Figure S2. The three-time EDS analysis of $MoSe_{2+x}$-rGO.

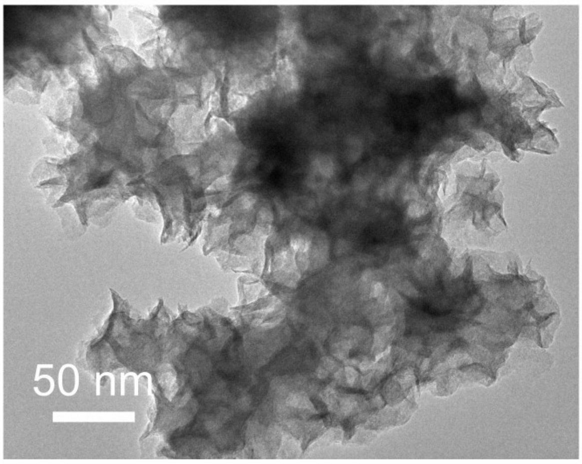

Figure S3. TEM image of $MoSe_{2+x}$-rGO.

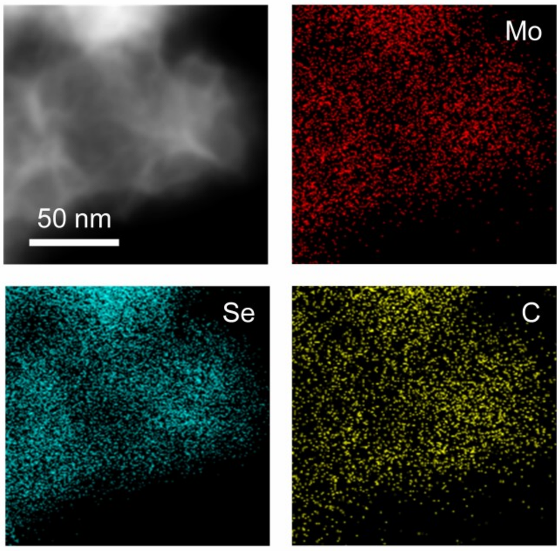

Figure S4. EDS mapping images of $MoSe_{2+x}$-rGO.

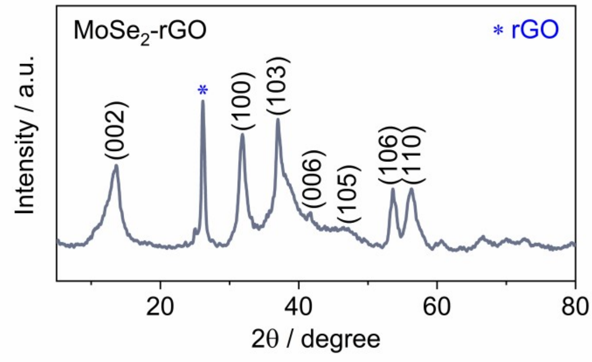

Figure S5. XRD spectrum of MoSe$_2$-rGO.

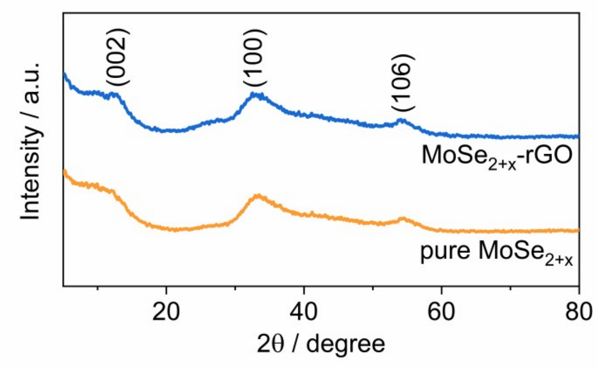

Figure S6. XRD spectra of MoSe$_{2+x}$-rGO and pure MoSe$_{2+x}$.

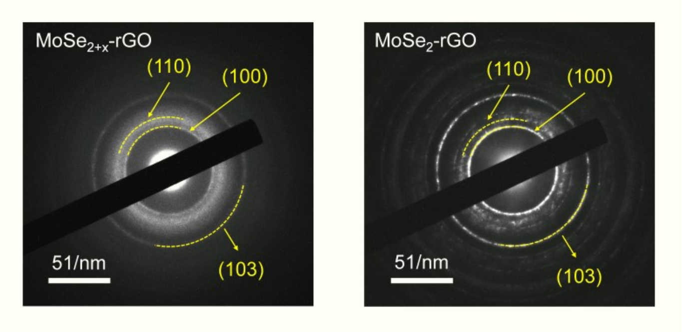

Figure S7. SAED patterns of $MoSe_{2+x}$-rGO and $MoSe_2$-rGO.

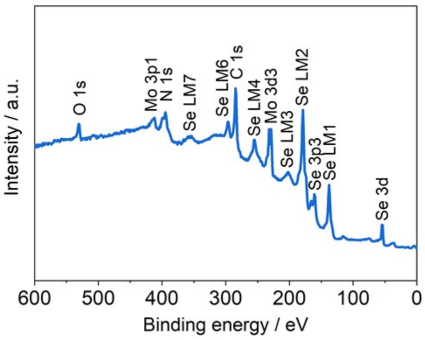

Figure S8. XPS spectrum of $MoSe_2$-rGO.

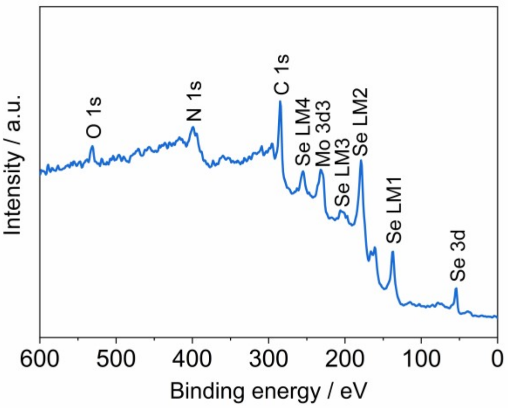

Figure S9. XPS spectrum of $MoSe_{2+x}$-rGO.

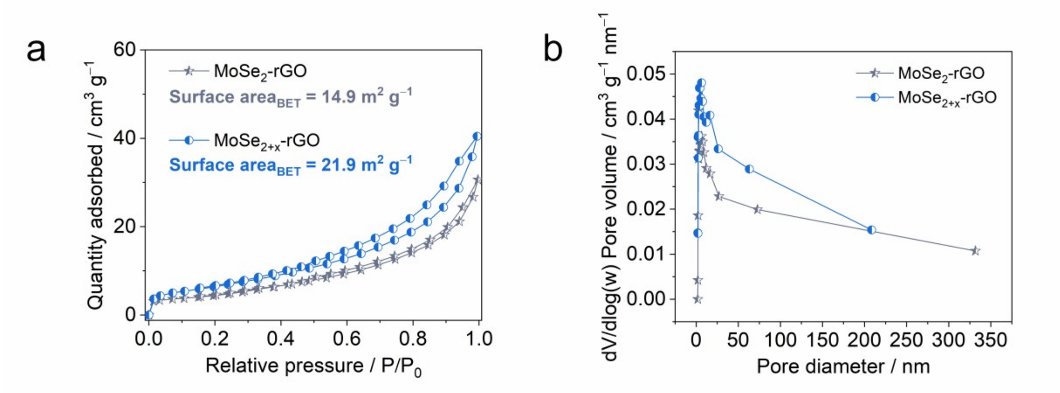

Figure S10. (a) Nitrogen adsorption/desorption isotherms. (b)The corresponding pore-size distribution curves.

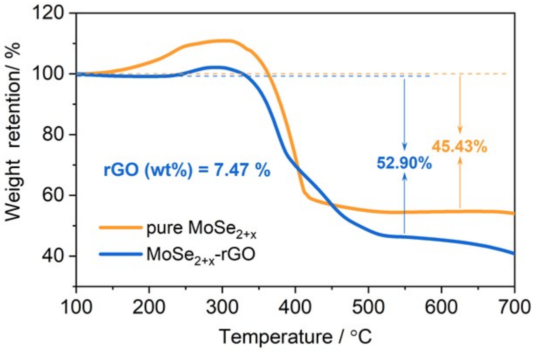

Figure S11. TGA of pure MoSe$_{2+x}$ and MoSe$_{2+x}$-rGO.

Section 6. Electrochemical performance of MoSe$_{2+x}$-rGO for PIBs

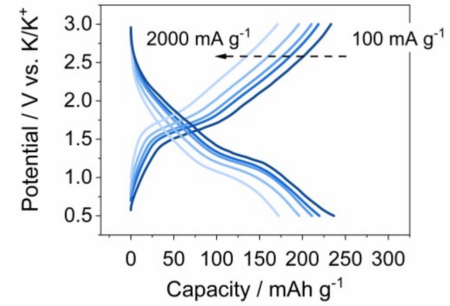

Figure S12. Typical discharge/charge profiles at different current densities of MoSe$_{2+x}$-rGO for PIBs.

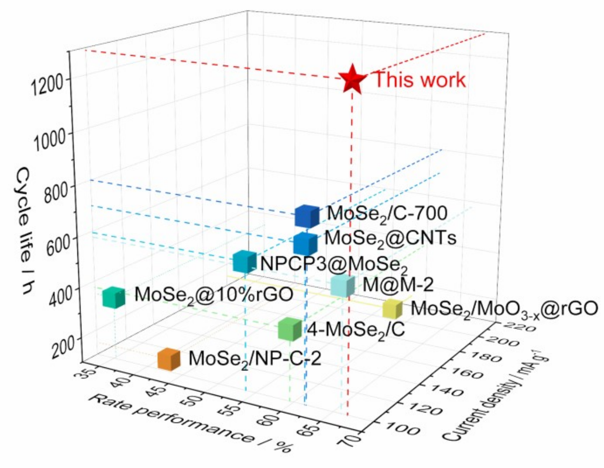

Figure S13. Comparisons of rate performance and cycle life with MoSe$_2$-based composites for PIBs.

Table S1. Rate performance and cycle life of $MoSe_2$-based composites and $MoSe_{2+x}$-rGO for PIBs.

Materials	Current densities (mA g^{-1})	Cycle Life (h)	Rate performance* (high/low current density (mA g^{-1})) (%)
$MoSe_{2+x}$-rGO (This work)	100	1290	66.8 (1000/100)
$MoSe_2$@10%rGO	100	350	35.3 (2000/500)
$MoSe_2$/C-700	100	800	61.6 (1000/100)
M@M-2	100	576	66.0 (1000/100)
NPCP3@$MoSe_2$	100	594	53.7 (1000/100)
$MoSe_2$/NP-C-2	100	150	43.1 (2000/100)
4-$MoSe_2$/C	100	375	59.5 (1000/100)
$MoSe_2$@CNTs	100	700	61.4 (1000/100)
$MoSe_2$/MoO_{3-x}@rGO	200	145	58.0 (1000/100)

*Rate performance: Capacity retention at high currents compared to low currents.

Section 7. Reaction mechanism of $MoSe_{2+x}$-rGO

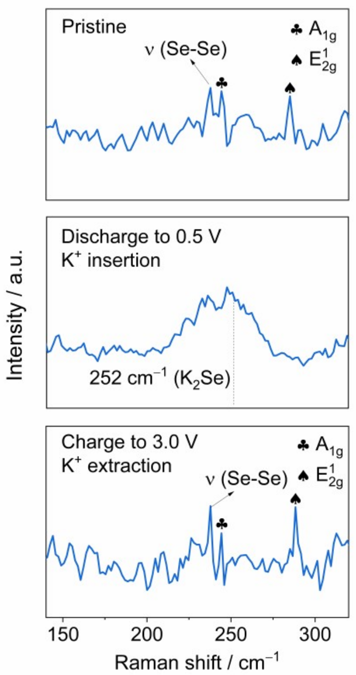

Figure S14. Raman spectra of pristine $MoSe_{2+x}$-rGO, $MoSe_{2+x}$-rGO discharged to 0.5 V and charged to 3.0 V for PIBs.

Section 8. Electrochemical kinetics of $MoSe_{2+x}$-rGO and $MoSe_2$-rGO

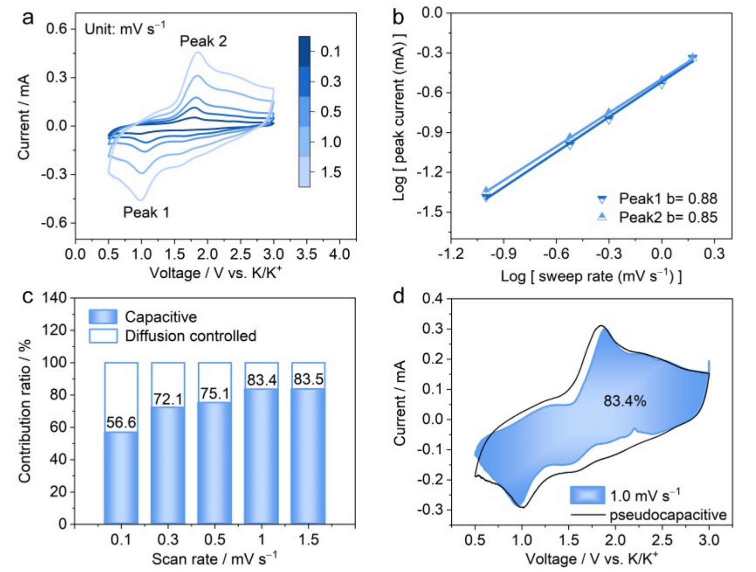

Figure S15. Electrochemical kinetics of $MoSe_{2+x}$-rGO for PIBs at different scan rates. (a) CV curves of $MoSe_{2+x}$-rGO at different scan rates. (b) Plot of log(i) vs log(v) and their fitting lines of $MoSe_{2+x}$-rGO calculated from CV curves. (c) Contribution ratio of pseudocapacitance of $MoSe_{2+x}$-rGO at different scan rates. (d) CV profile with the pseudocapacitive contribution of $MoSe_{2+x}$-rGO at scan rate of 1.0 mV s^{-1}.

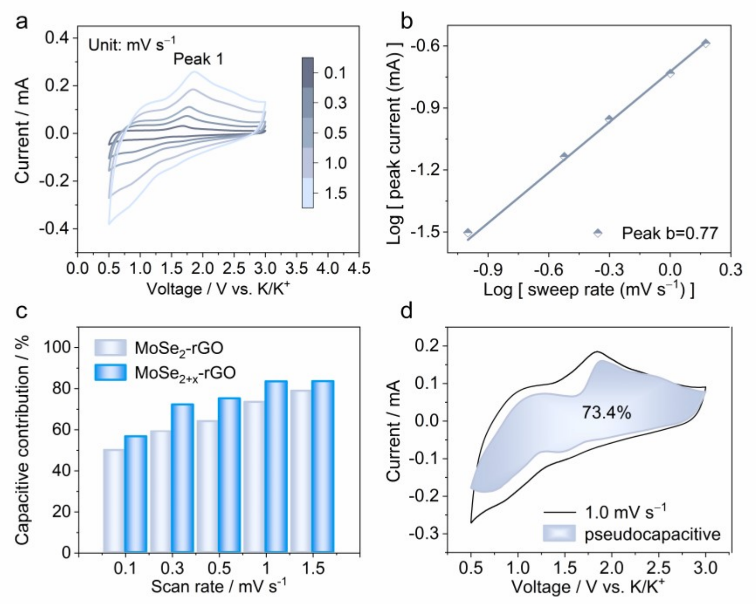

Figure S16. Electrochemical kinetics of MoSe$_2$-rGO for PIBs at different scan rates. (a) CV curves of MoSe$_2$-rGO at different scan rates. (b) Plot of log(i) vs log(v) and their fitting line of MoSe$_2$-rGO calculated from CV curves. (c) Contribution ratio of pseudocapacitance of MoSe$_2$-rGO and MoSe$_{2+x}$-rGO at different scan rates. (d) CV profile with the pseudocapacitive contribution of MoSe$_2$-rGO at scan rate of 1.0 mV s^{-1}.

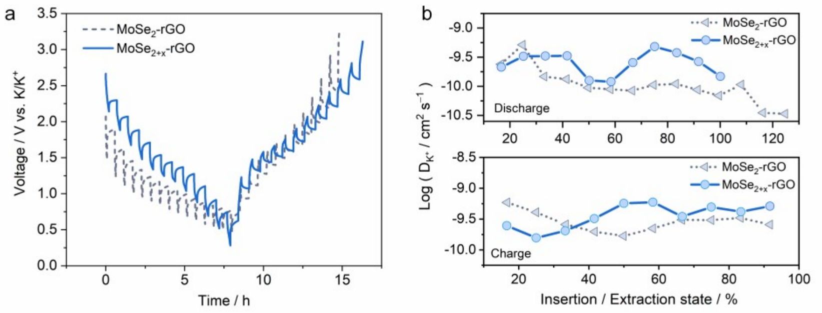

Figure S17. (a) Galvanostatic intermittent titration technique (GITT) curves of $MoSe_{2+x}$-rGO and $MoSe_2$-rGO. (b) The K^+ diffusion coefficient of $MoSe_{2+x}$-rGO and $MoSe_2$-rGO during charging/discharging.

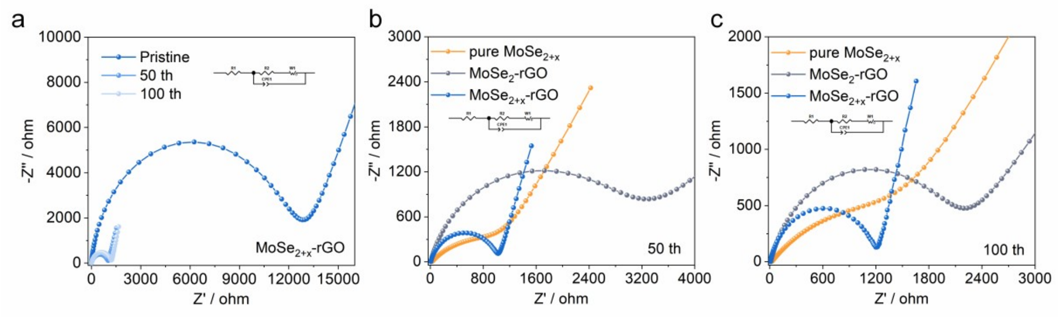

Figure S18. Nyquist plots of pure MoSe$_{2+x}$, MoSe$_{2+x}$-rGO and MoSe$_2$-rGO before and after cycling.

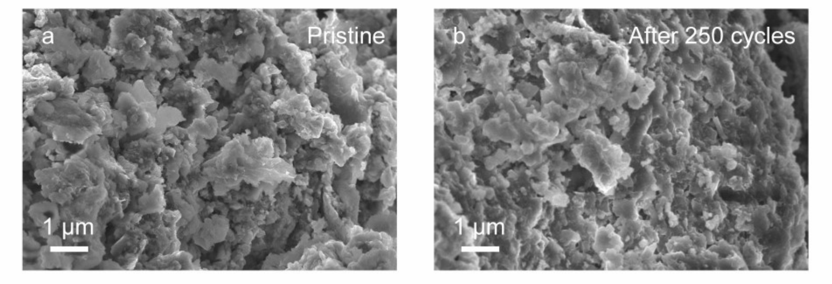

Figure S19. The SEM images of (a) the pristine $MoSe_{2+x}$-rGO electrode and (b) the electrode after 250 cycles.

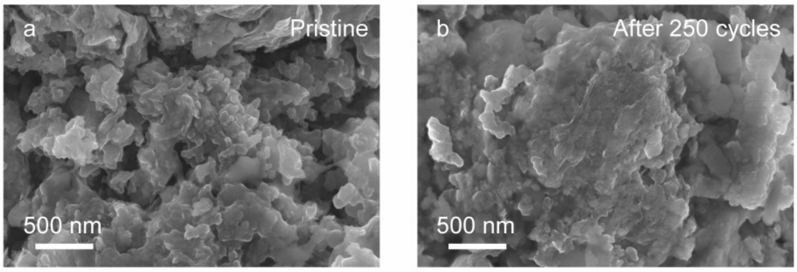

Figure S20. The SEM images of (a) the pristine $MoSe_2$-rGO electrode and (b) the electrode after 250 cycles.

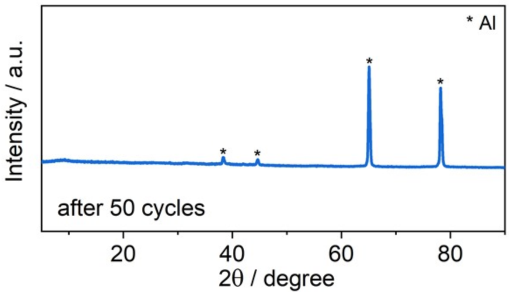

Figure S21. XRD spectrum of $MoSe_{2+x}$-rGO coated on Al foil after 50 cycles at 500 mA g^{-1}.

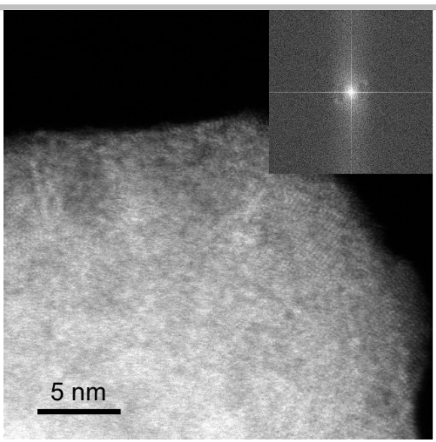

Figure S22. HRTEM image of $MoSe_{2+x}$-rGO after 50 cycles at 500 mA g^{-1}.

Section 9. Electrochemical performance of full cell for PIBs

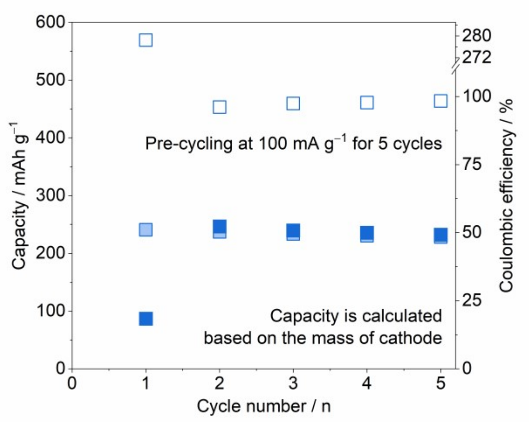

Figure S23. Pre-cycling at 100 mA g^{-1} for 5 cycles of $MoSe_{2+x}$-rGO||NG full cell.

Section 10. Electrochemical performance of $MoSe_{2+x}$-rGO for LIBs

Table S2. Rate performance of Se-based cathodes and $MoSe_{2+x}$-rGO for LIBs.

Materials	Rate performance* (high/low current density (mA g^{-1})) (%)	Ref.
$MoSe_{2+x}$-rGO	85 (1000/100)	This work
Li_2Se-MH	70.9 (1000/100)	[6]
Bi_2Se_{3-x}/NC	78.9 (1C/0.1C)	[7]
SeS_2 with GST	74 (1000/100)	[8]
Se_xS_{8-x}-M52/VACNTs	68.2 (1000/100)	[9]
$MoSe_2$@rGO/S	61.2 (1C/0.12C)	[10]
$MoSe_2$/N-rGO/S	52.1 (1C/0.1C)	[11]

*Rate performance: Capacity retention at high currents compared to low currents.

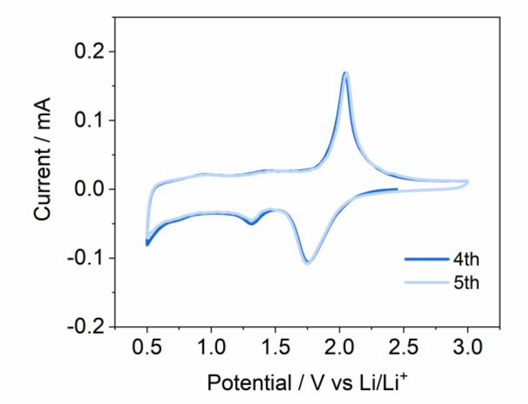

Figure S24. CV curves of $MoSe_{2+x}$-rGO at 0.1 mV s^{-1} for LIBs.

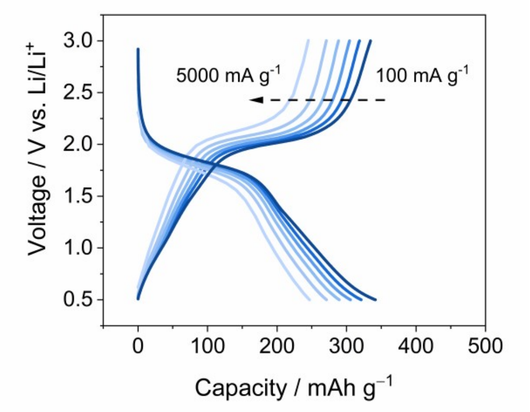

Figure S25. Typical discharge/charge profiles at different current densities of $MoSe_{2+x}$-rGO for LIBs.

References

1. G. Kresse and J. Furthmüller, Efficient iterative schemes for ab initio total-energy calculations using a plane-wave basis set, *Phys. Rev. B*, 1996, **54**, 11169-11186.
2. J. Hafner, Ab-initio simulations of materials using VASP: Density-functional theory and beyond, *J. Comput. Chem.*, 2008, **29**, 2044-2078.
3. P. E. Blöchl, Projector augmented-wave method, *Phys. Rev. B*, 1994, **50**, 17953-17979.
4. J. P. Perdew, K. Burke and M. Ernzerhof, Generalized Gradient Approximation Made Simple, *Phys. Rev. L*, 1996, **77**, 3865-3868.
5. E. Caldeweyher, S. Ehlert, A. Hansen, H. Neugebauer, S. Spicher, C. Bannwarth and S. Grimme, A generally applicable atomic-charge dependent London dispersion correction, *J. Chem. Phys.*, 2019, **150**, 154122.
6. C. W. Lu, W. K. Zhang, R. Y. Fang, Z. Xiao, H. Huang, Y. P. Gan, J. Zhang, X. P. He, C. Liang, D. M. Zhu and Y. Xia, Facile and efficient synthesis of Li_2Se particles towards high-areal capacity Li_2Se cathode for advanced Li–Se battery, *Sustain. Mater. Technol.*, 2021, **29**, e00288.
7. S. S. Qiu, X. Q. Liang, S. W. Niu, Q. G. Chen, G. M. Wang and M. H. Chen, Quantitative defect regulation of heterostructures for sulfur catalysis toward fast and long lifespan lithium-sulfur batteries, *Nano Res.*, 2022, DOI: 10.1007/s12274-022-4453-9.
8. Y. Zhang, Y. Guo, B. Y. Wang, Y. H. Wei, P. Jing, H. Wu, Z. D. Dai, M. Wang and Y. Zhang, An integrated hybrid interlayer for polysulfides/selenides regulation toward advanced Li–SeS_2 batteries, *Carbon*, 2020, **161**, 413-422.
9. H. N. Fan, S. L. Chen, X. H. Chen, Q. L. Tang, A. P. Hu, W. B. Luo, H. K. Liu and S. X. Dou, 3D Selenium Sulfide@Carbon Nanotube Array as Long-Life and High-Rate Cathode Material for Lithium Storage, *Adv. Funct. Mater.*, 2018, **28**, 1805018.
10. W. Z. Tian, B. J. Xi, Z. Y. Feng, H. B. Li, J. K. Feng and S. L. Xiong, Sulfiphilic Few-Layered $MoSe_2$ Nanoflakes Decorated rGO as a Highly Efficient Sulfur Host for Lithium-Sulfur Batteries, *Adv. Energy Mater.*, 2019, **9**, 1901896.
11. H. L. Wong, X. W. Ou, M. H. Zhuang, Z. J. Liu, M. D. Hossain, Y. T. Cai, H. W. Liu, H. Lee, C. Z. Wang and Z. T. Luo, Selenium Edge as a Selective Anchoring Site for Lithium–Sulfur Batteries with $MoSe_2$/Graphene-Based Cathodes, *ACS Appl. Mater. Interfaces*, 2019, **11**, 19986-19993.